Development of thermal barrier coating systems from Al microparticles. Part I: Influence of processing conditions on the mechanisms of formation

Germain Boissonnet, Benjamin Grégoire, Gilles Bonnet, Fernando Pedraza

HAL Id: hal-02542049
https://hal.science/hal-02542049

Submitted on 14 Apr 2020

Development of thermal barrier coating systems from Al microparticles.
Part I: Influence of processing conditions on the mechanisms of formation

Germain Boissonnet*, Benjamin Grégoire, Gilles Bonnet, Fernando Pedraza

Laboratoire des Sciences de l'Ingénieur pour l'Environnement, (LaSIE, UMR-CNRS 7356), Université de La Rochelle, Avenue Michel Crépeau, 17042 La Rochelle Cedex 1, France

* Corresponding author: boissonnet.germain@gmail.com

Abstract. This work presents the mechanisms of formation on pure nickel of full thermal barrier coating systems (aluminide coating, thermally grown oxide and thermal barrier top coating) from micro-sized Al particles dispersed in a slurry annealed in different atmospheres (Ar, synthetic air, water vapour and mixtures thereof). The simultaneous formation of nickel aluminides and of a thermal barrier made of sintered hollow alumina spheres involved self-propagating high-temperature synthesis in all conditions. However, the microstructures and adherence of the top coatings changed markedly with either a diffusion step (700°C-2 h) or a complete heat treatment (700°C-2 h + 1100°C-2 h) depending on the atmosphere. Whereas fast consumption of Al occurred in Ar to form the nickel aluminides, synthetic air and water vapour fostered the peripheral oxidation of Al micro-sized particles that impeded the release of Al and its diffusion towards the substrate. This resulted in heterogeneous diffusion layers but thicker top coatings with better sintering and thicker alumina shells.

Keywords: aluminizing; thermal barrier coating; nickel; oxidation; diffusion; slurry

1. Introduction

Current processes of fabrication of thermal barrier coatings (TBCs) for the hottest sections of aeronautical engines are very complex and quite expensive. Therefore, they cannot be applied to other sections that now require thermal insulation due to the increase of the turbine inlet temperatures. Among the alternative coating techniques, slurries containing Al microspheres appear particularly attractive as they can form a top foam of hollow alumina microspheres in addition to an aluminide coating [1-5]. It has been demonstrated that just a 40 µm -thick top foam indeed confers thermal insulation equivalent to those of 400 µm thick conventional plasma-sprayed coatings made of yttria-stabilized zirconia between 400°C and 900°C [6]. However, this light alumina foam is not sufficiently mechanically resistant and can be easily removed, for example by grit blasting [7]. Pedraza and Podor investigated the influence of annealing conditions on the formation of hollow alumina spheres from micro-sized Al particles [8]. The release of Al from the particles was associated with two simultaneous mechanisms: i) peripheral

oxidation of the spheres and ii) volume expansion of the Al core upon heating [8,9]. Their findings were in agreement with the pioneer works of Levitas et al. for micro-sized particles [10-12]. They reported that the initial amorphous alumina shell surrounding the microparticles grows upon heating until it reaches a critical thickness of 4 to 5 nm [13,14]. At about 550°C, the amorphous alumina shell therefore crystallizes into γ-Al$_2$O$_3$ [13,15,16]. Since the density of γ-Al$_2$O$_3$ is greater than that of the amorphous alumina layer [9,17], tensile stresses develop in the newly formed γ-Al$_2$O$_3$ layer, inducing nano-cracks in the alumina shell. Depending on the p_{O_2} and on the heating ramp, healing of the non-continuous alumina shell may occur by oxidation of the exposed Al core [12]. When the temperature approaches the Al melting point, additional tensile stresses develop on the γ-Al$_2$O$_3$ layer since the solid-liquid transformation of Al is accompanied with a volume expansion of 12 % [18]. The release of Al from the particles is therefore controlled by the simultaneous healing of the alumina shell and the diffusion of Al through the cracks because of the pressure build-up in the molten Al core [9,10,12]. The thickness of the oxide shell exerts a tremendous effect on the amount of Al flowing out from the microspheres. The size of the microparticles also has a considerable influence on the kinetics of oxidation (i.e. growth of the peripheral alumina layer) and on the release of Al [13,19]. This can be attributed to the higher specific surface area of the smaller particles, which simultaneously enhance their peripheral oxidation and limit the expansion of the Al melt [13,21]. The peripheral oxide layer of the smaller particles tend to resist more to the pressure build-up induced by the thermal expansion of the Al melt upon heating [9,18] and could provide a significant source to thicken the particles walls and to enhance the sintering of the top coating when a sufficient p_{O_2} or p_{H_2O} is employed for the heat treatment. In contrast, large particles tend to be better Al donors for the formation of the diffusion coating as the release of Al would be faster. Indeed, the larger the Al core, the higher the pressure build-up on the oxide shell [9,21]. In this view, Kolarik et al. found that the optimal particle size was in the range of 2-5 µm to simultaneously obtain continuous diffusion zones and adherent ceramic top coatings from organic-based slurries [4].

The mechanisms of formation of water-based Al-containing slurry coatings have already been discussed under inert atmosphere (Ar) [2,3,20] and in air [1] on pure nickel and on nickel-based superalloys. However, none of such studies investigated the influence of the atmosphere on the simultaneous aluminizing of the substrate and the sintering of the hollow alumina spheres. Therefore, the present study aims at elucidating the influence of the atmosphere on the mechanisms of formation of the complete thermal barrier coating systems. Pure nickel was used as a model material for nickel-based superalloys. One inert atmosphere (Ar) and two oxidizing atmospheres (synthetic air and Ar-10% H$_2$O) were investigated.

2. Experimental procedure

Approximately 2 mm-thick coupon samples were prepared from a 12.7 mm diameter nickel rod (99.98 % purity, GoodFellow). After machining, the samples were ground with SiC paper to P180 grade, rinsed with deionized water and ultrasonically cleaned in ethanol. The water-based slurries were prepared with deionized water (solvent), polyvinyl alcohol (organic binder) and micro-sized Al particles. Two different types of Al powders were used in this study: i) microparticles of homogeneous sizes (**Al_HS**), provided by Sibthermochim (Russia), and ii) microparticles of dispersed sizes (**Al_DS**), provided by Hermillon (France). The Al_DS powders exhibited a mean diameter of ~3 µm while the Al_HS powders were measured to be ~8 µm. Particle size distribution for both types of powders is presented in **Figure 1**. The Al_DS particles showed a higher dispersion of the particle diameter than the Al_HS. Slurry amounts of 9±1 mg.cm^{-2} were deposited on the samples by air brush. The samples were coated on both sides and dried in a fume cupboard for 1 h after slurry deposition. After drying, deposit thicknesses were measured via cross-section analysis to be ~55 µm and ~50 µm for Al_DS and Al_HS particles respectively.
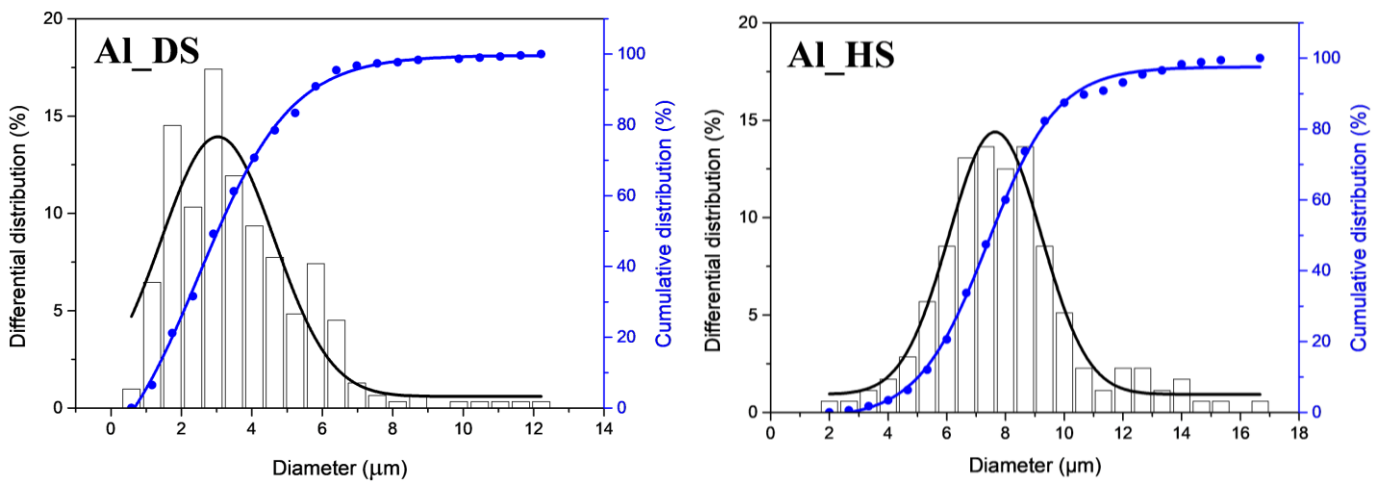

Figure 1 – Size distribution of the Al powders investigated in the study.

A SETARAM TGA 92 thermobalance with a 1 µg accuracy was used for the heat treatment in Ar and in synthetic air, while a SETARAM Setsys Evo 1750 (0.1 µg accuracy) was used for the heat treatment under wet Ar (10 vol.% water vapour). The water vapour was created using the SETARAM Wetsys module and transferred to the bottom of the thermal enclosure of the thermobalance via a heated transfer pipe. Three different atmospheres were investigated in this study: one inert (Ar) and two oxidizing atmospheres (synthetic air and Ar-10 vol. % H$_2$O). For the sake of clarity, the latter will be noted Ar-10%H$_2$O. Since the heating ramp has a strong influence on the simultaneous peripheral oxidation and opening of the Al microparticles [8,15], all the heating ramps were fixed at 5°C/min (**Figures 2a** and **2b**). The samples were systematically cured at 400°C for 1 h to remove the organic binder prior to any further

step [22]. For a better understanding of the mechanisms of formation, one or two additional steps were then performed based on previous works done in our group [2,3]: the diffusion step (700°C-2 h) to aluminize the substrate by major inward diffusion of Al, and the annealing step (1100°C-2 h) to stabilize the nickel aluminide coating (i.e. to promote the outward diffusion of nickel) and to stabilize the α-Al_2O_3. **Table 1** summarizes the different experimental conditions tested for the diffusion heat treatment (**Figure 2a**) and the complete heat treatment (**Figure 2b**). For both heat treatments, the coated samples were exposed to three different atmospheres (Ar, synthetic air and Ar-10% H_2O).
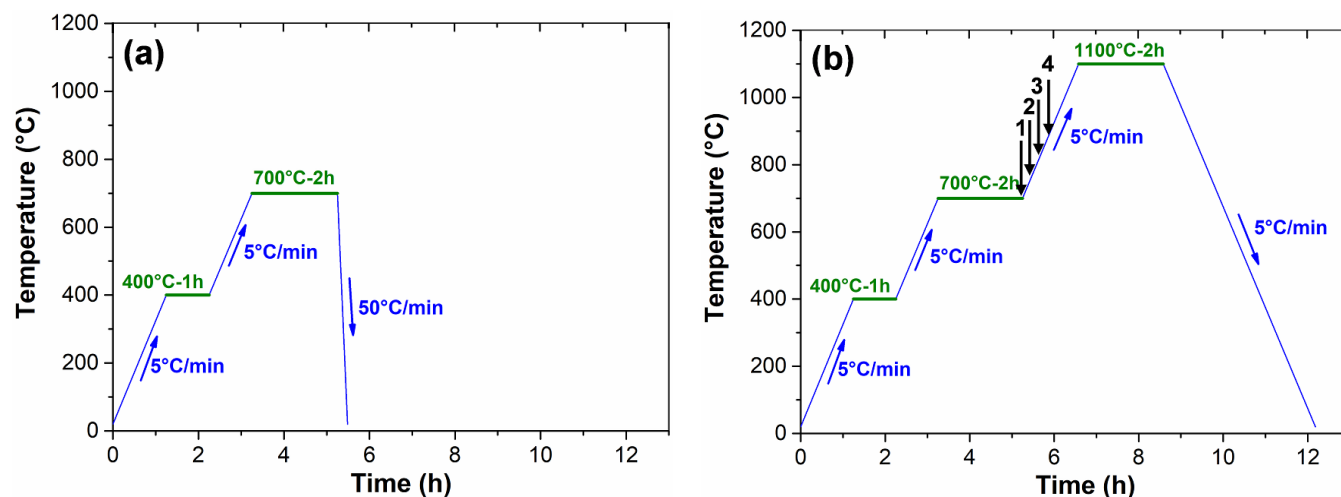

***Figure 2** – Temperature profiles of (**a**) the diffusion heat treatment and (**b**) the complete heat treatment performed in TGA to form the thermal barrier systems on pure nickel. The arrow marks (1 to 4) in Figure 1b indicate the introduction of the oxidizing atmosphere at the expense of Ar.*

***Table 1** – Summary of the different heat treatments performed in TGA (see Figure 2).*

Heat Treatment	Starting atmosphere	Introduction of the oxidizing atmosphere	Mark in *Figure 1*b
400°C-1 h + 700°C-2 h	Ar Synthetic air Ar-10% H_2O	-	-
400°C-1 h + 700°C-2 h + 1100°C-2 h	Ar Synthetic air Ar-10% H_2O	-	-
	Ar	550°C 600°C 650°C 700°C	1 2 3 4

Additional samples were first treated in Ar before the introduction of the oxidizing atmosphere (synthetic air or Ar-10% H_2O) upon heat treatment (Table 1). Here, the objective was to propose a single heat treatment to elaborate a complete thermal barrier coating system (diffusion coating + thermally grown oxide + ceramic top coating) by switching the composition of the atmosphere during the heat

treatment. The corresponding switch between the inert and the oxidizing atmosphere is indicated with the arrow marks (1 to 4) in **Figure 2b**.

The observations of the surface and of the cross-sections were performed with a FEI Quanta 200F environmental scanning electron microscope (SEM) equipped with Schottky Field Emission Gun (FEG) at 0.9 mbar. All the SEM images shown in this work were taken in the backscattered electron (BSE) mode. The chemical analysis by Energy Dispersive Spectrometry (EDS) were obtained through an EDAX detector coupled to the SEM. X-ray diffraction (XRD) was conducted in the Bragg-Brentano configuration with a Bruker AXS D8 Advance diffractometer using Cu $K_{\alpha 1}$ radiation ($\lambda = 0.15406$ nm) to characterize the oxide and the intermetallic crystal structures.

3. Results

3.1. *Microstructure of the thermal barrier systems after the diffusion heat treatment (700°C-2 h)*

Figure 3 presents the macrographs and the morphologies of the two different types of Al microparticles (Al_HS and Al_DS) from the slurry coated pure nickel samples exposed to the diffusion heat treatment in the three different atmospheres (Ar, synthetic air and Ar-10%H_2O). The corresponding XRD patterns of the different surfaces are presented in **Figure 4**. **Figure 5** shows the cross-sections of the coatings.
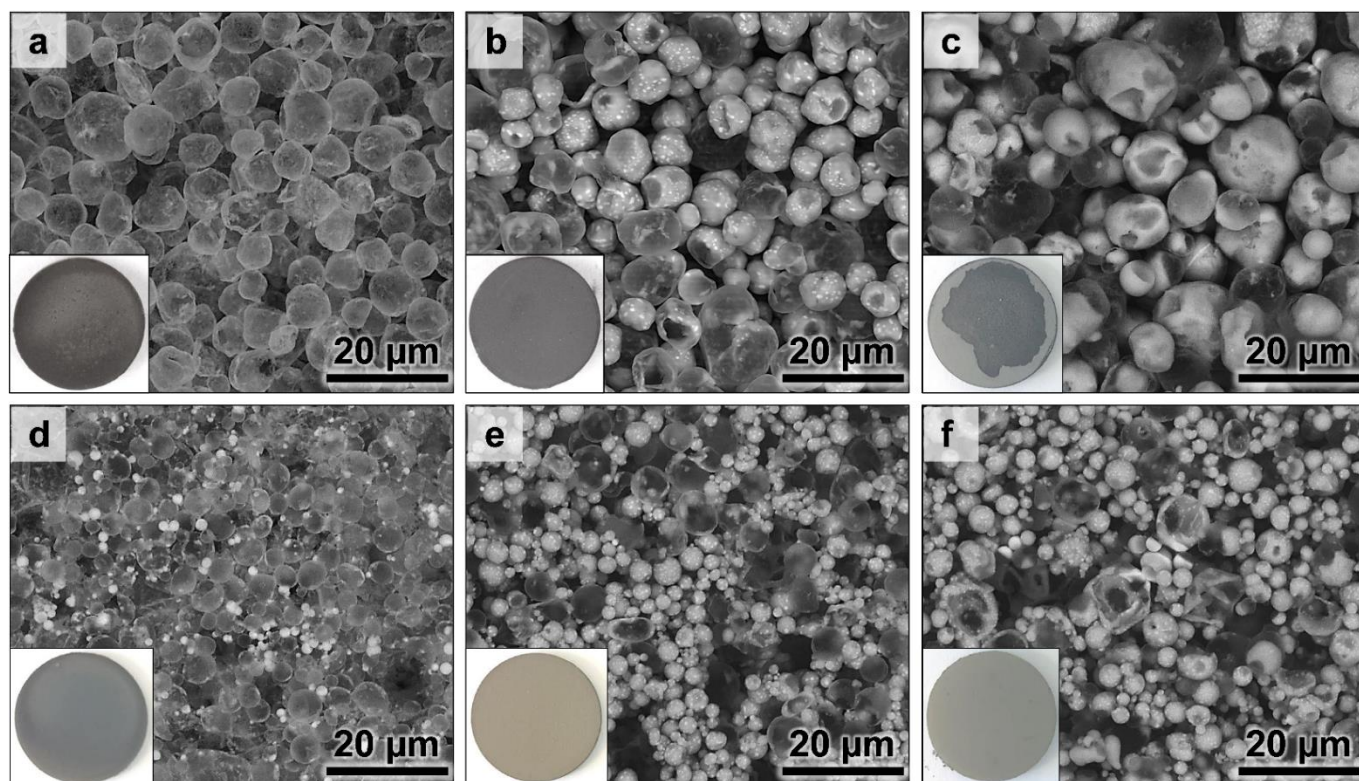

Figure 3 *– Surface morphology of the thermal barrier systems elaborated from (**a, b, c**) Al_HS and (**d, e, f**) Al_DS microparticles on pure nickel after the diffusion heat treatment (700°C-2 h) in (**a, d**) Ar, (**b, e**) synthetic air and (**c, f**) Ar-10%H_2O. The macros of the surfaces are shown in the insets.*

Under Ar flow (**Figure 3a**), the surface of the sample coated with Al_HS slurry is composed of hollow spheres featuring thin transparent shells. No X-ray peak related to Al can be observed in the patterns (**Figure 4a**) suggesting that the whole Al reacted with nickel upon the diffusion heat treatment. This is also confirmed by the fact that no metallic Al was observed in the cross-section of the top coating (**Figure 5a**). Al_HS particles led to a ceramic top layer of ~50 µm with hollow spheres that are observed on top of a continuous diffusion layer of ~50 µm. Whereas the δ-Ni_2Al_3 phase represents most of the diffusion layer for both types of slurry (identified via XRD **Figure 4a**), β-NiAl and γ'-Ni_3Al are successively identified at the interface with the nickel substrate (**Figure 5a**). In the case of the Al_DS slurry, the smallest particles (appearing bright in BSE mode) kept their Al core (**Figures 3d** and **5d**) and a small diffraction peak of Al is observed on the corresponding XRD pattern (**Figure 4b**). However, the identification of the δ-Ni_2Al_3 crystal structure indicates that most of the Al (i.e. the largest particles) had reacted with the Ni substrate. The hollow particles that were close to the substrate did not keep their spherical shape and started to collapse, hence leading to a thinner top coating of ~30 µm (**Figure 5d**).
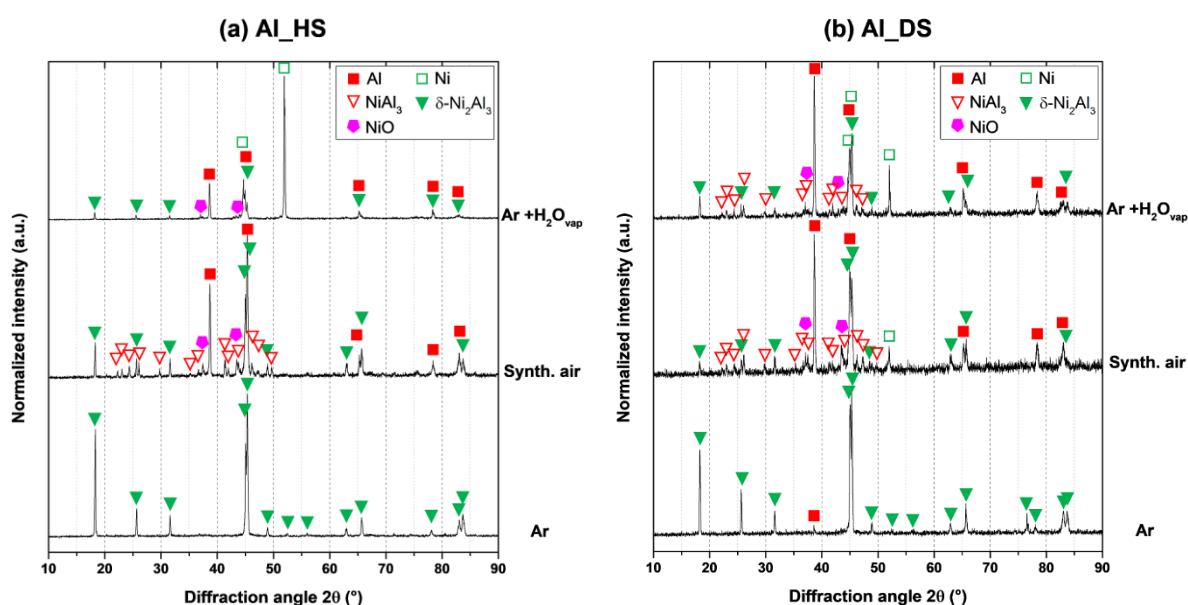

***Figure 4** – X-ray diffraction patterns of the slurry coated samples after the diffusion heat treatment (700°C-2 h) in Ar, synthetic air and Ar-10%H_2O for **(a)** Al_HS and **(b)** Al_DS microparticles.*

For the samples exposed to synthetic air, a large quantity of metallic Al is still present in the top coating for both the HS and the DS slurries (**Figure 4**). From the SEM observations (**Figures 3b** and **3e**), it appears that the larger microparticles are broken whereas the smaller ones are still filled with Al. These filled microparticles are also observed on the cross-sections of the Al_HS (**Figure 5b**) and the Al_DS samples (**Figure 5e**). The crystal structure of δ-Ni_2Al_3 identified on the XRD pattern indicates that the reaction between Al and Ni occurred in synthetic air too. The bright spots observed on the smaller microparticles (**Figures 3b, 3e, 5b** and **5e**) correspond to nickel enrichment according to the EDS spot

analyses and to the XRD analyses from which the crystal structure of $NiAl_3$ was identified. In addition, the X-ray peaks of NiO (**Figure 4**) indicate that the Ni from the substrate coated with the two slurries was oxidized during this 2 h step at 700°C. NiO indeed started to develop in the uncoated regions where the Al did not react with Ni to form the aluminide coating, as observed in **Figure 5e**. The exposure to synthetic air disturbed the supply of Al towards the substrate hence resulting in a thinner diffusion layer for the Al_HS sample (**Figure 5b**) and in the formation of diffusion islands for the Al_DS one (**Figure 5e**).
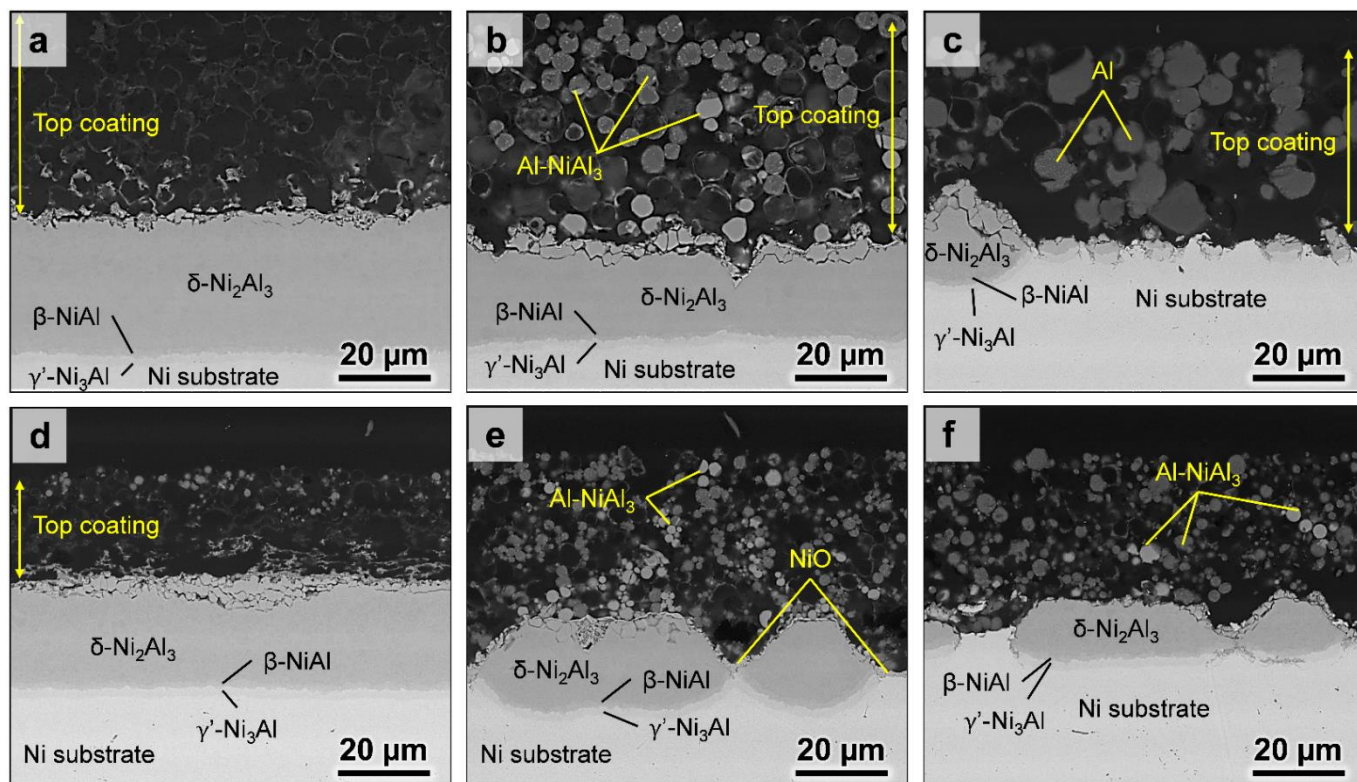

Figure 5 *– BSE cross-section images of the thermal barrier systems elaborated from (**a, b, c**) Al_HS and (**d, e, f**) Al_DS microparticles on pure nickel after the diffusion heat treatment (700°C-2 h) in (**a, d**) Ar, (**b, e**) synthetic air and (**c, f**) Ar-10%H_2O.*

The samples exposed to Ar-10%H_2O (**Figures 3c**, **3f, 5c** and **5f**) exhibit less emptied particles than when exposed to synthetic air, hence a larger ratio of large particles still contains Al (**Figure 6**). However, in these conditions, the Al_HS top coating spalled almost completely from the substrate and remained adherent only to the edges of the sample (**Figure 3c**). The XRD pattern for this Al_HS sample (**Figure 4a**) shows much greater intensities for the peaks of Ni and of Al with respect the intensity of the δ-Ni_2Al_3 peaks. In contrast, no detachment is observed in the Al_DS sample for which Ni and Al are also observed along with the $NiAl_3$ and δ-Ni_2Al_3 phases (**Figure 4b**). The diffusion layers of the two types of samples appear very heterogeneous due to the insufficient release of Al from the particles (**Figures 5c** and **5f**). Moreover, there are less bright spots associated with Ni enrichment in Ar-10%H_2O than in Ar

and in synthetic air. Further, the top coating shows a poorer contact with the substrate in water vapour than in Ar and in air irrespective of the particle size. This probably explains the spallation of the Al_HS top coating observed on **Figure 3c**. In contrast, barely any NiO grew in the uncoated regions after exposure to Ar-10%H_2O (**Figure 4**). The reason for this will be discussed in section 4.1.

In order to assess the impact of the particle size and of the atmosphere on the aluminization of pure Ni, the particle size distribution of emptied particles (Al_HS and Al_DS) as a function of particle size after the diffusion heat treatment (700°C-2 h) in the three different atmospheres is plotted in **Figure 6**. The particle size values corresponding to 0, 50 and 100% of emptied particles for the different conditions are given in **Table 2**. Regardless of the atmosphere composition and of the type of Al microparticles, the larger particles generally broke more rapidly than the smaller ones (i.e. higher fraction of emptied particles). For the Al_HS microparticles, the whole Al reservoir reacted with nickel after the diffusion heat treatment in Ar (**Figure 6a**). This is also observed for Al_DS microparticles except for the particles smaller than 3 µm that kept their Al core (**Figures 3d** and **6b**). By performing the heat treatment in Ar, the major Al supply from the microspheres therefore led to the formation of relatively thick and homogeneous diffusion layers on pure nickel substrate (**Figures 5a** and **5d**).

By performing the diffusion heat treatment in synthetic air or in Ar-10%H_2O, fewer particles released their Al and the threshold for the opening of the microspheres shifted towards larger-sized particles for both Al_HS (**Figure 6a**) and Al_DS slurries (**Figure 6b**), in particular for the Al_HS microparticles (**Table 2**). This is illustrated on the surface (**Figure 3c**) and in the cross-section (**Figure 5c**) micrographs for pure nickel coated with the Al_HS particles and exposed to the diffusion heat treatment in Ar-10%H_2O where a significant fraction of the larger microparticles did not release their Al. Since fewer particles released their Al source in both synthetic air and Ar-10%H_2O, fewer interactions between Al and Ni were made possible leading to the discontinuous diffusion layers observed previously.
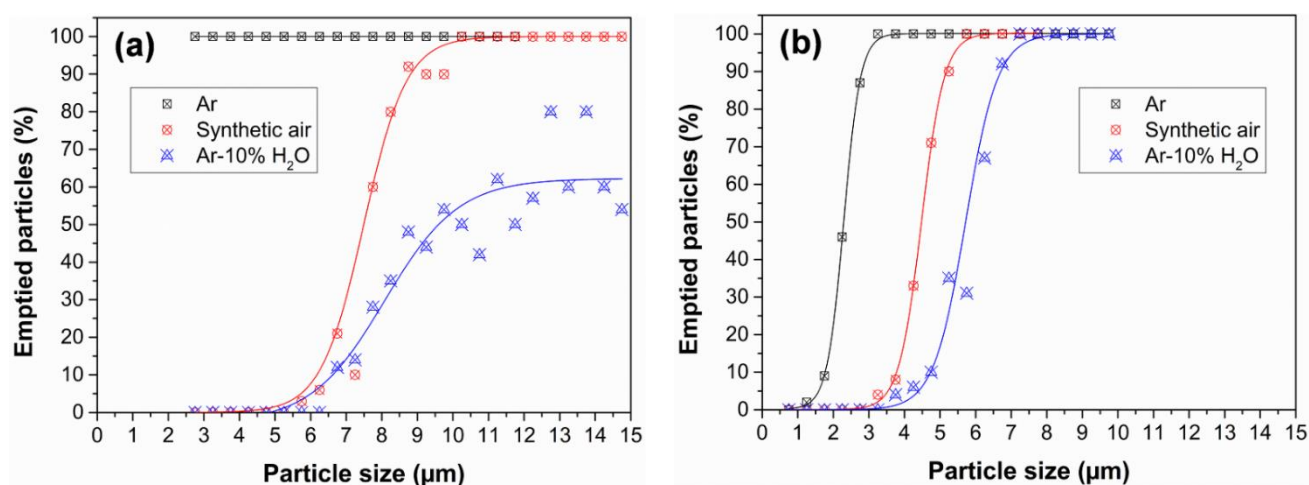

Figure 6 – Distribution of the emptied particles as a function of particle size after the diffusion heat treatment (700°C-2 h) in Ar, synthetic air and Ar-10%H_2O for (a) Al_HS and (b) Al_DS microparticles.

Table 2 – *Determination of the particle size (μm) for 0, 50 and 100% of emptied particles for the two types of Al microparticles after the diffusion heat treatment (700°C-2 h) in Ar, synthetic air and Ar-10%H_2O.*

Atmosphere	Al_HS			Al_DS		
	0%	50%	100%	0%	50%	100%
Ar	-	-	> 2.5	< 1.5	2.3	> 3
Synthetic air	< 4.5	7.5	> 10.5	< 3.0	4.5	> 6
Ar-10%H_2O	< 5.0	9.6	-	< 3.5	5.7	> 7.5

3.2. Microstructure of the thermal barrier systems after the complete heat treatment (700°C-2 h + 1100°C-2 h)

The surfaces and the morphologies of the samples coated with the Al_HS and Al_DS slurries after the complete heat treatment in the different atmospheres are given in **Figure 7**. The corresponding XRD patterns are presented in **Figure 8**. Cross-sectional micrographs of the coatings are presented in **Figure 9**.
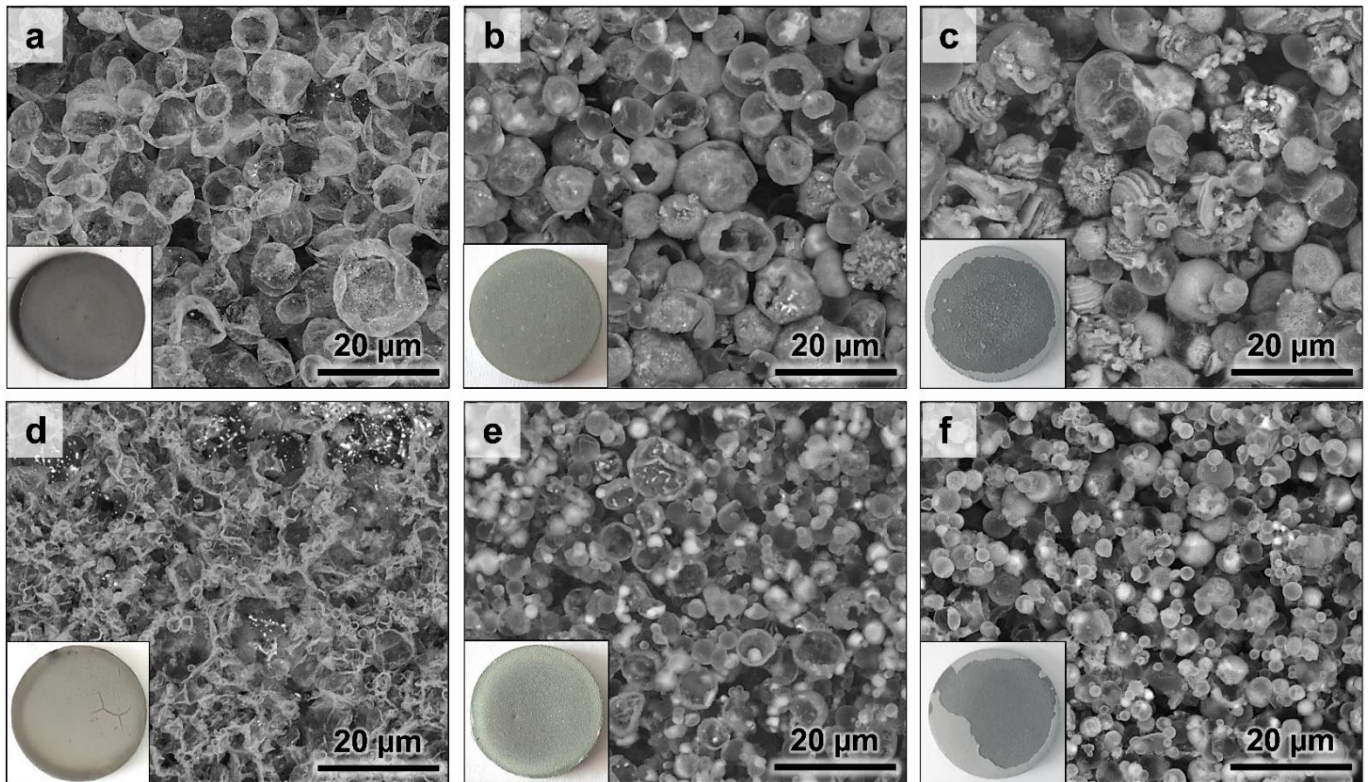

Figure 7 – *Surface morphology of the thermal barrier systems elaborated from (**a, b, c**) Al_HS and (**d, e, f**) Al_DS microparticles on pure nickel after the complete heat treatment (700°C-2 h + 1100°C-2 h) in (**a, d**) Ar, (**b, e**) synthetic air and (**c, f**) Ar-10%H_2O. The macros of the surfaces are shown in the insets.*

Under Ar flow, the hollow spheres from the Al_HS slurry shrunk and lost their initial shape (**Figure 7a**) whereas the Al_DS microparticles completely lost their spherical shape and collapsed to form a thin layer through which the metallic sub-layer is visible (**Figure 7d**). The corresponding macrograph of the latter shows a "dry-mud" like morphology in which the top coating is broken by multiple micro-cracks. The diffusion coatings are similar for both samples and constituted of two different layers: an external

layer composed of both β-NiAl and γ'-Ni$_3$Al phases and an internal layer that corresponds to the γ'-Ni$_3$Al composition at the interface with the nickel substrate (**Figures 9a and 9d**) while neither Al nor δ-Ni$_2$Al$_3$ could be identified via XRD (**Figure 8**). By contrast, the microstructure of the top coating composed of α-Al$_2$O$_3$ (see XRD in **Figure 8**) is significantly different for the two types of microparticles. Whereas the broken spheres from the top coating collapsed in the case of Al_DS particles (**Figure 9d**) to give a very thin top coating (~10 µm), the Al_HS particles maintained a quasi-spherical shape with a thin oxide shell for a resulting top coating of ~30 µm (**Figure 9a**).
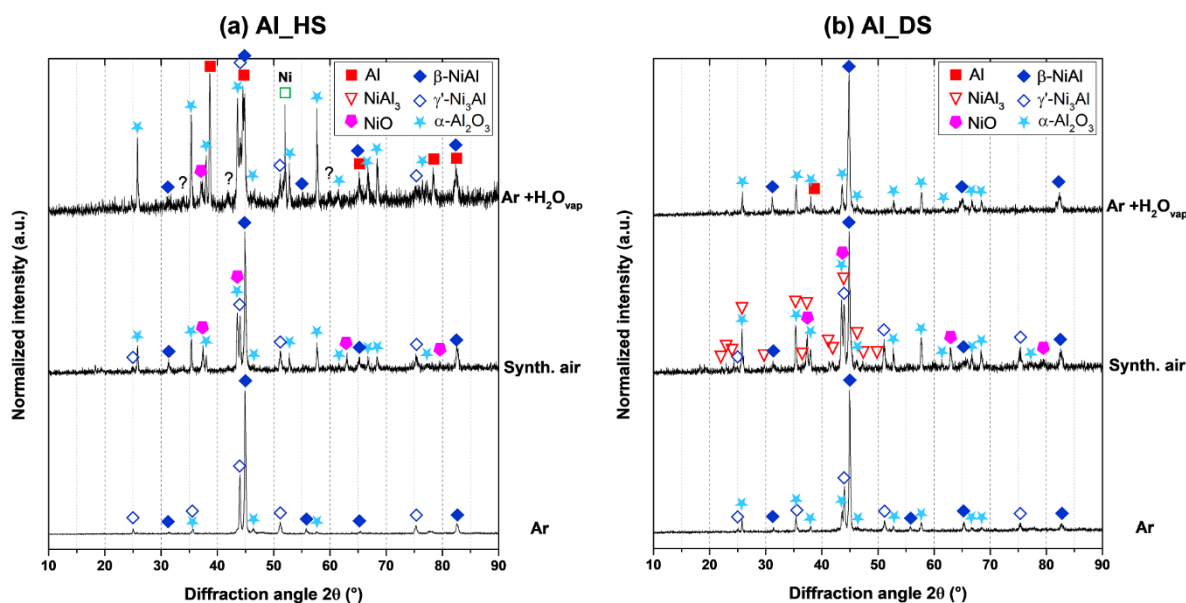

Figure 8 *– X-ray diffraction patterns of the slurry coated samples after the complete heat treatment (700°C-2 h + 1100°C-2 h) in Ar, synthetic air and Ar-10%H$_2$O for (**a**) Al_HS and (**b**) Al_DS microparticles.*

For the samples heat treated in synthetic air (**Figures 7b** and **7e**), the microspheres are less deformed and appear more sintered than the ones obtained in Ar. Moreover, the oxide crusts exhibit a marked thickening of the alumina shells. This thickening led to thicker top coating (**Figures 9b** and **9e**) and is in good agreement with the XRD patterns since the characteristic diffraction peaks of α-Al$_2$O$_3$ are unambiguously observed (**Figure 8**). Like with Ar, the crystal structures of Al and δ-Ni$_2$Al$_3$ are no longer identified on the XRD pattern of both samples whereas both β-NiAl and γ'-Ni$_3$Al ones are detected after the complete heat treatment (**Figure 8**). The bright spots (BSE mode) observed on the surface of Al_HS particles (**Figure 7b**) and of Al_DS particles (**Figure 7e**) correspond to unemptied Al microparticles enriched in Ni, confirmed by the top coatings cross-sections (**Figures 9b** and **9e**) and the detection of NiAl$_3$ in addition to β-NiAl and γ'-Ni$_3$Al (**Figure 8b**). Also, the annealing at 1100°C in synthetic air brings about the formation of a relatively thick thermally grown Al$_2$O$_3$ oxide (TGO). However, the substrate was vulnerable to oxidation and gave thick NiO oxide scale while an alumina layer started to internally develop around the diffusion islands between the diffusion spots (**Figures 9b** and **9e**).

The top coatings of both Al_HS and Al_DS samples heat treated in Ar-10%H_2O spalled off. One shall note that the observations of the microspheres of the surfaces (**Figures 7c** and **7f**) and of the cross-sections (**Figure 9c** and **9f**) were made on the edges of the samples where the top coatings remained adherent. The microparticles of the Al_HS slurry exhibit various oxide morphologies and appear more oxidized than after the heat treatment under synthetic air. As a matter of fact, a small fraction of the large particles seems to have broken to release Al from the core. Unlike with synthetic air, Ni, Al and $NiAl_3$ were identified by XRD for the Al_HS sample (**Figure 8a**), indicating that some Al remained trapped in the top coating. Like with synthetic air, the surface of both coatings displays brighter contrasted areas rich in Ni (**Figure 7**). Moreover, no NiO was detected by XRD for both Al_HS and Al_DS samples and only the structure of α-Al_2O_3 was observed (**Figures 8a** and **8b**). The heat treatment in water vapour resulted in a more heterogeneous diffusion of Al that gave smaller and dispersed diffusion islands composed of β-NiAl which were also surrounded by an α-Al_2O_3 oxide layer.
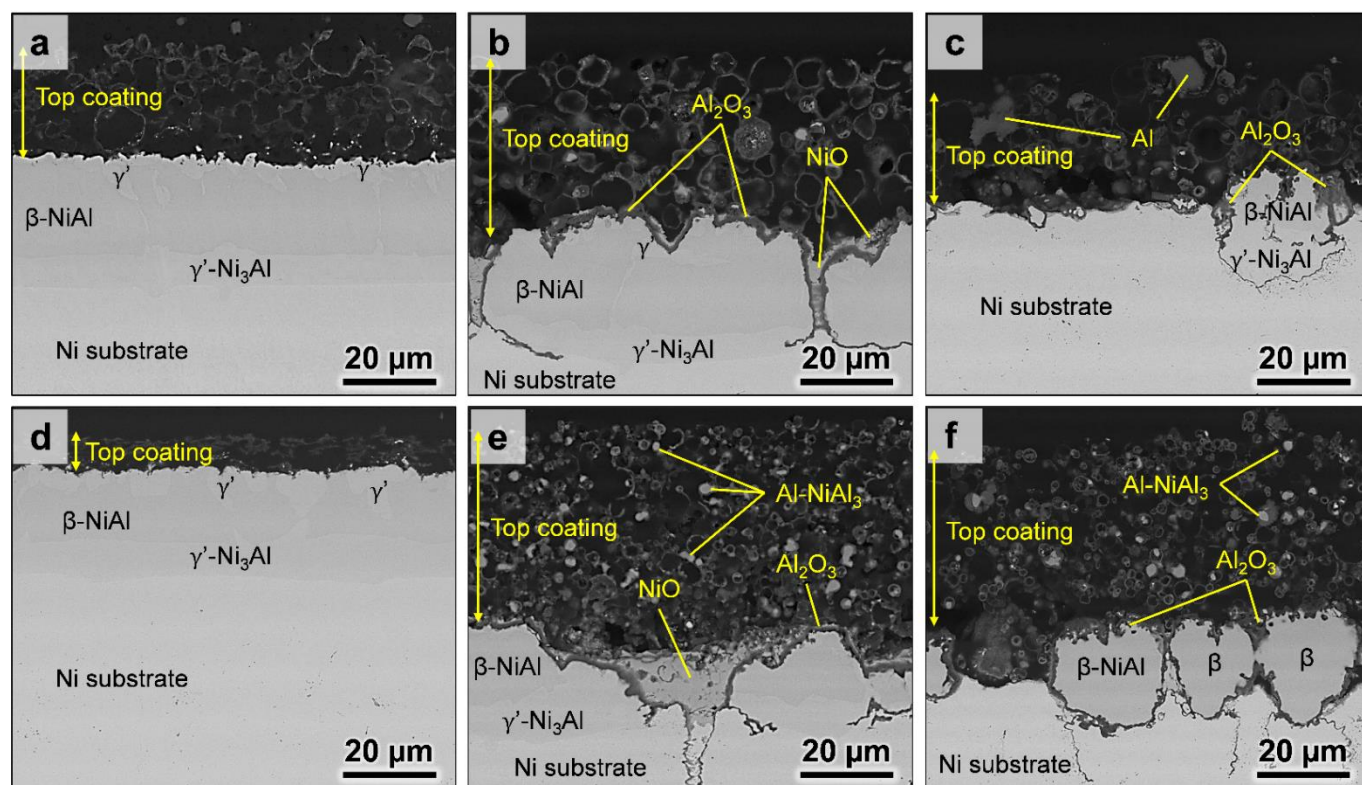

Figure 9 – *BSE cross-section images of the thermal barrier systems elaborated from (**a, b, c**) Al_HS and (**d, e, f**) Al_DS microparticles on pure nickel after the complete heat treatment (700°C-2 h + 1100°C-2 h) in (**a, d**) Ar, (**b, e**) synthetic air and (**c, f**) Ar-10%H_2O.*

The evolution of the mass gain with the annealing time in the different atmospheres is depicted in **Figure 10**. Clearly, the very small mass gain values observed in Ar (~0.5 mg) is in line with the poor oxidation observed for the Al microparticles and the substrate. However, the use of synthetic air or of Ar-10%H_2O brings about an overall mass gain much greater (~7.5 mg) than in Ar at the end of the

experiment. This agrees with the thick oxide crusts observed for the particles in the corresponding top coatings (see **Figures 9b**, **9c**, **9e** and **9f**).
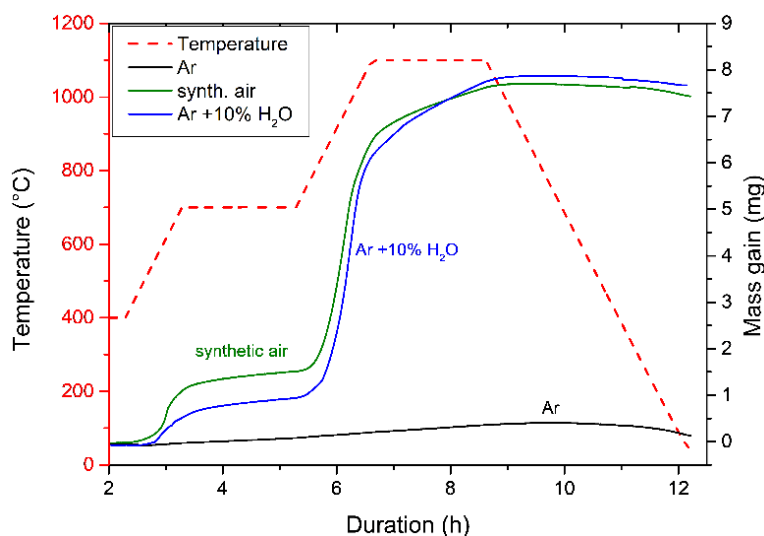

Figure 10 – *Mass gain curves obtained by TGA of the slurry coated samples (Al_HS on one face and Al_DS on the other) heat treated in Ar, synthetic air and Ar-10%H_2O.*

3.3. Microstructure of the thermal barrier systems with switch of atmospheres upon heating

The replacement of the inert Ar atmosphere by an oxidizing atmosphere was performed at different times along the heat treatment (see **Table 1**). Thus, synthetic air was introduced at 550, 600, 650 and 700°C during the heating ramp from 400 to 700°C while the Ar-10%H_2O atmosphere was introduced only at 600 and 650°C.

The introduction of synthetic air at 550 or 600°C results in coatings similar to the ones obtained with the heat treatment under full synthetic air, regardless of the type of microparticles (**Figures 11a** and **11d**). An overall mass gain of ~7.5 mg was recorded for both samples with introduction of synthetic air at 550 or 600°C (**Figure 12**). This value is also equivalent to the one obtained for the sample fully heat treated in synthetic air. Diffusion islands composed of β-NiAl and of γ'-Ni_3Al grew over a continuous γ'-Ni_3Al diffusion layer. A relatively thick α-Al_2O_3 TGO developed on top of the nickel aluminide phases whereas NiO formed between the diffusion islands and at the interface with the top coatings (**Figures 11a** and **11d**). The top coatings achieved with the switch at 550 or 600°C are composed of sintered hollow alumina spheres with thick oxide shells, whose thicknesses are comparable with the ones of the samples fully treated in synthetic air. In the same way as the full heat treatment in synthetic air, a poor interface between the top layer and the aluminide coating is observed for both Al_DS and Al_HS samples that resulted in spallation of the top coating for the Al_HS one (**Figure 11a**).

When synthetic air was introduced at 650°C (**Figures 11b** and **11e**), the diffusion coatings obtained from both types of microparticles were more homogeneous and similar to the ones produced in the inert

Ar atmosphere (**Figures 9a** and **9d**). However, as opposed to the latter, the top coatings exhibit thicker shells and a thicker α-Al$_2$O$_3$ TGO at the interface between the nickel aluminide coating and the top coating. This is confirmed by the maximum mass gain value of ~3 mg (**Figure 12**) that is lower than the ones of the samples with synthetic air introduced at 550 or 600°C, but that is also significantly higher than the one of the sample heat treated in Ar.

The introduction of synthetic air at 700°C also resulted in coatings similar to the ones obtained with the full heat treatment in Ar and, therefore, the diffusion layers appear homogeneous for both types of microparticles. In contrast, the shells of the top coating are very thin, resulting in shrunk top coatings, with collapsed microspheres for Al_DS microparticles (**Figure 11f**). However, a slight oxidation is to be highlighted as the overall mass gain value (~2 mg) was observed to be significantly higher than the sample heat treated in Ar (**Figure 12**).
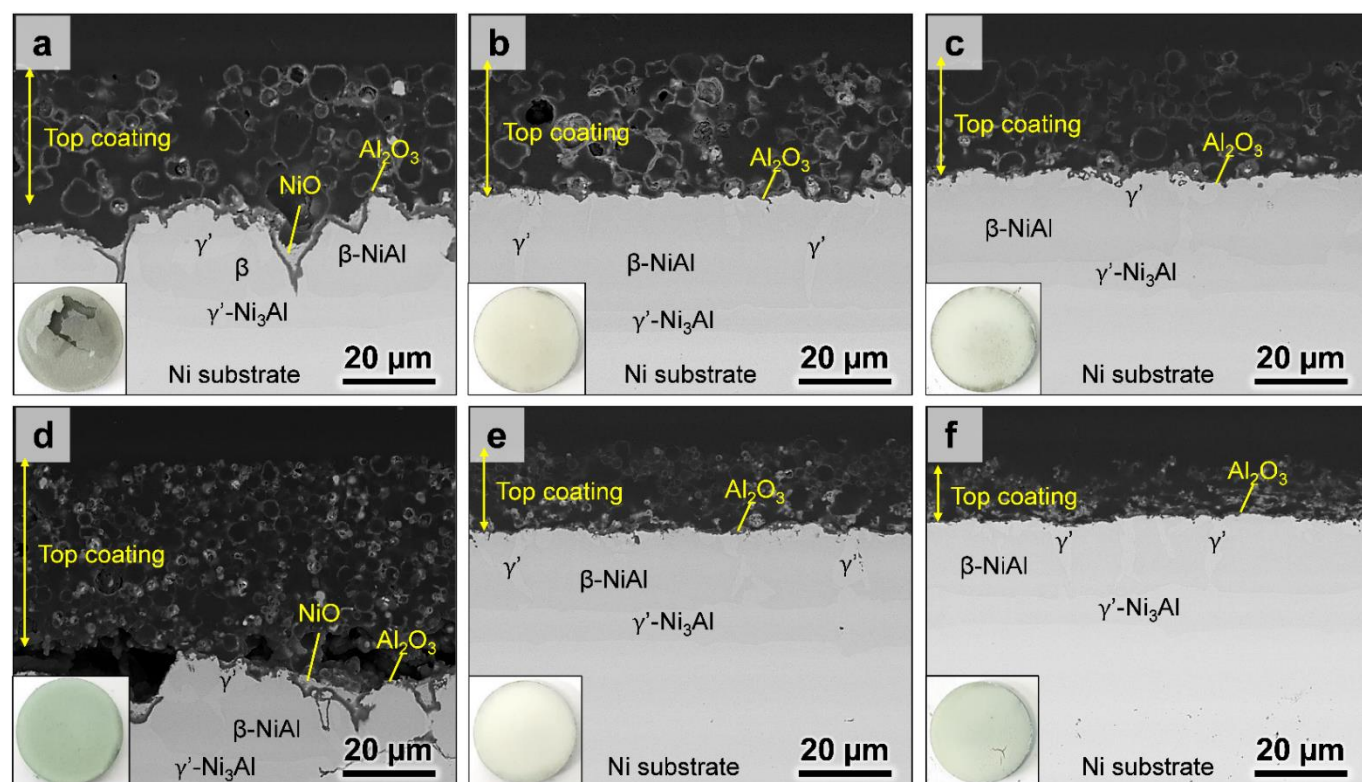

Figure 11 – BSE cross-section images and corresponding surface macrographs of the thermal barrier systems elaborated from (a, b, c) Al_HS and (d, e, f) Al_DS microparticles on pure nickel after introduction of synthetic air at (a, d) 600°C, (b, e) 650°C and (c, f) 700°C, and subsequent annealing (700°C-2 h + 1100°C-2 h). The macros of the surfaces are shown in the insets.

Figure 13 shows the cross-section of the coatings with the introduction of Ar-10%H$_2$O at 650°C (**Figures 13a** and **13c**) and at 700°C (**Figures 13b** and **13d**). The top coatings were not fully adherent to the surface when Ar-10%H$_2$O was introduced at 650°C (**Figures 13a** and **13c**) while at 700°C they spalled off completely with the Al_HS or remained adhered with the Al_DS particles. All the diffusion

layers had approximately the same thickness and comprised β-NiAl as the main phase and γ'-Ni$_3$Al at the grain boundaries. However, the diffusion layers were quite uneven and internally oxidized with the switch to Ar-10%H$_2$O for both Al_HS and Al_DS samples at 650°C and for the Al_HS sample at 700°C (**Figures 13a**, **13b** and **13c**). Contrarily, the introduction of water vapour at 700°C for the Al_HS sample resulted in a homogeneous diffusion coating (**Figure 13d**).

Figure 12 *– Mass gain curves obtained by TGA of the slurry coated samples (Al_HS on one face and Al_DS on the other) heat treated in different atmospheres – switch from Ar to synthetic air.*
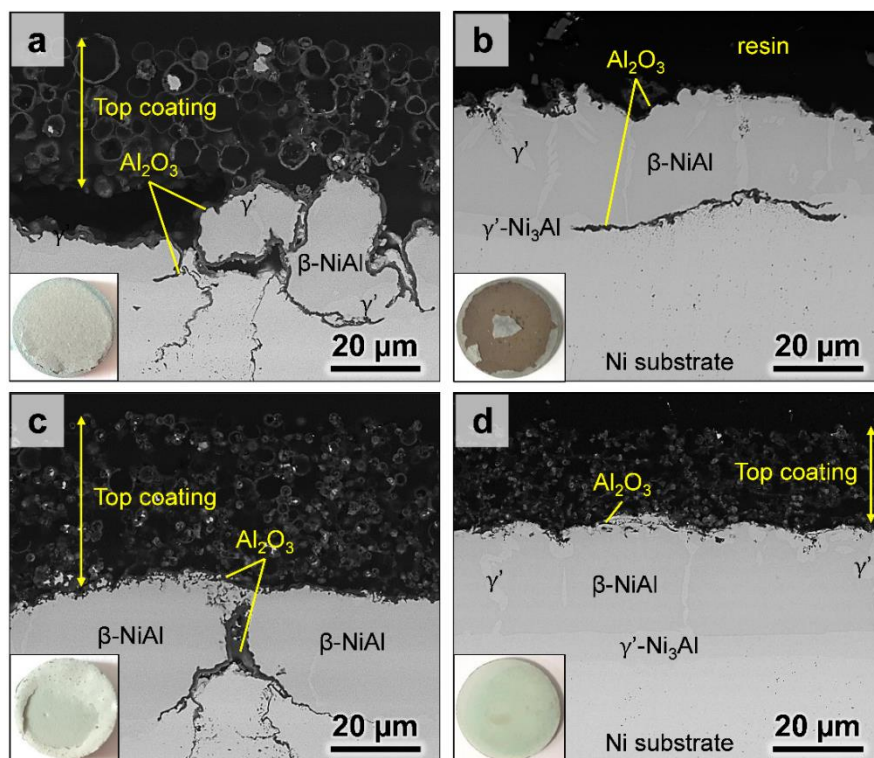
Figure 13 *– BSE cross-section images and corresponding surface macrographs of the thermal barrier systems elaborated from (**a, b**) Al_HS and (**c, d**) Al_DS microparticles on pure nickel after introduction of Ar-10%H$_2$O at (**a, c**) 650°C and (**b, d**) 700°C, and subsequent annealing (700°C-2 h + 1100°C-2 h).*

Figure 14 compares the mass gain curves of the samples heat treated in Ar, in Ar-10%H_2O and with the introduction of Ar-10%H_2O at 650 or 700°C. When Ar-10%H_2O is introduced at 700°C, the mass gain increases markedly upon heating to 1100°C but slows down when this temperature is reached. A similar effect is observed when the wet Ar is introduced at 650°C but the overall mass gain is greater than at 700°C. Therefore, thicker oxide shells are observed in the top coatings when Ar-10%H_2O is introduced at 650°C (**Figure 13a** and **Figure 13c**).
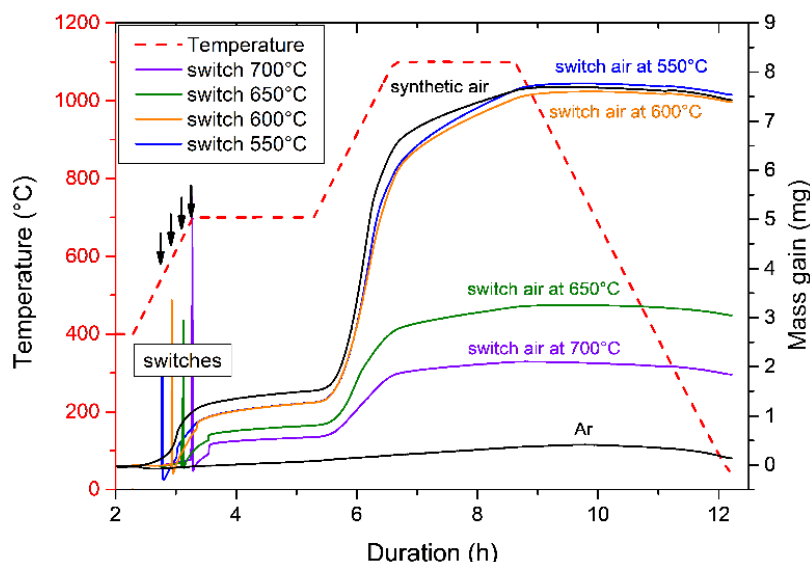

Figure 14 – *Mass gain curves obtained by TGA of the slurry coated samples (Al_HS on one face and Al_DS on the other) heat treated in different atmospheres – switch from Ar to Ar-10%H_2O.*
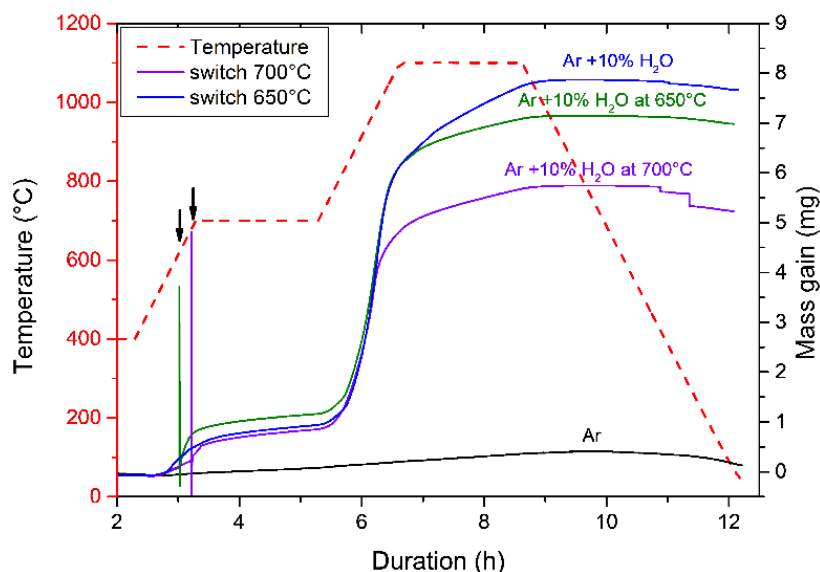
4. Discussion

4.1. Single atmosphere for the formation of thermal barrier systems

Under Ar atmosphere, the Al microspheres tend to release their Al core rapidly while limited oxidation occurs due to the low oxygen and water partial pressures contained in the commercial gas (2 vpm O_2 + 3 vpm H_2O according to the supplier). Although some Al was still trapped in the smallest particles of the Al_DS slurry (<3 µm) after the diffusion heat treatment (see **Figure 6**), most of the Al of both Al_HS and Al_DS samples was released towards the substrate and reacted with Ni to form aluminide coatings of ~30 µm thickness following self-propagating high temperature synthesis (SHS) mechanisms [3,20]. The δ-Ni_2Al_3 phase that represented most of the diffusion layer for both types of slurry after the diffusion step (see **Figures 5a** and **5d**) transformed into β-NiAl and γ'-Ni_3Al phases after the 1100°C-2 h annealing step (see **Figures 9a** and **9d**) due to solid-state interdiffusion between Al and Ni as commonly observed for high-activity Al coatings [23-25]. Similar microstructures were reported on pure nickel when slurry coated with comparable Al microparticles and annealed in Ar [2]. Concerning the

top coating, both types of microparticles led to alumina hollow spheres with thin transparent shells after the diffusion heat treatment (**Figures 5a** and **5d**). With the annealing step at 1100°C for 2 h, the top coatings got thinner (~10 µm and ~30 µm for Al_DS and Al_HS, respectively – see **Figures 9a** and **9d**) and micro-cracks appeared for the Al_DS sample (**Figure 7d**), although they were still observed to be adherent on the samples. The thinning and cracking of the coatings was attributed to the volume shrinkage of the thin alumina shells that occurs during the γ-Al_2O_3 to α-Al_2O_3 transition [9,21,26]. The same morphology was reported by Pedraza and Podor after exposure to 1150°C in 120 Pa He-4%H_2 atmosphere [8].

When increasing the oxidizing ability of the atmosphere using synthetic air (p_{O_2} ~ 0.20 atm) or Ar-10%H_2O (p_{O_2} ~0.05 atm), the microspheres tend to keep more Al (see **Figure 6**). As a matter of fact, the threshold for the opening of the microspheres shifted towards larger-sized particles by performing the diffusion heat treatment in synthetic air or in Ar-10%H_2O, regardless of the type of Al microparticles (**Table 2**). This is attributed to the greater peripheral oxidation of Al microparticles in both oxidizing atmospheres than in inert Ar atmosphere, as reported in Ref. [8]. This greater oxidation is highlighted on the mass gain curves of **Figure 10** by a significant increase of mass from approximately 550°C whereas no marked evolution is observed in Ar. Such increase of mass is usually associated with the crystallization of the amorphous alumina layer into γ-Al_2O_3 [13,15,19]. Since fewer particles released their Al source, fewer interactions between Al and Ni were made possible leading to discontinuous diffusion layers after the diffusion heat treatment (**Figures 5b**, **5c**, **5e** and **5f**). After the additional annealing step at 1100°C for 2 h, the quantity of Al that diffused towards the substrate did not significantly increase and inter-diffusion between Al and Ni converted δ-Ni_2Al_3 into β-NiAl and γ'-Ni_3Al (**Figures 9b**, **9c**, **9e** and **9f**). Alternatively, the presence of the $NiAl_3$ structure for the Al_DS sample (**Figure 8**) and the bright particles observed within the top coatings (**Figures 9b**, **9c**, **9e** and **9f**) indicate that some Al remained trapped in the particles and could thus not diffuse towards the substrate. The large mass gains observed upon heating between 700 and 1100°C in synthetic air and in Ar-10%H_2O (**Figure 10**) can therefore be attributed to the fast oxidation of the Al melt eventually released through the cracks of the shells [19,26]. This would explain the formation of quite thick oxide crusts [9,27] and the high level of sintering of the top coatings after the complete heat treatment in both synthetic air (**Figures 7b** and **7e**) and Ar-10%H_2O (**Figures 7c** and **7f**). Note that the further thickening and sintering of the hollow alumina spheres most probably hampered their shrinkage [9,21] by comparison with the ones formed in Ar [8]. As a result, thicker top coatings were obtained in both oxidizing atmospheres (**Figures 9b**, **9c**, **9e** and **9f**) than in Ar (**Figures 9a** and **9d**). Synthetic air and Ar-10%H_2O also fostered the growth of the α-Al_2O_3 TGO in comparison to Ar (see cross-section images of **Figure 9**).

The differences between the heat treatment in synthetic air and in Ar-10%H_2O mostly lie in the oxidation behaviour of the particles and of the substrate as emphasized on the mass gain curves of **Figure 10**. As a matter of fact, synthetic air generated more oxidation of the slurry coated samples than Ar-10%H_2O after the diffusion step at 700°C for 2 h. Since no NiO was observed after the diffusion heat treatment in Ar-10%H_2O, this difference is mainly attributed to the formation of NiO on the uncoated regions of the samples exposed to synthetic air, as observed in **Figure 5e**. Despite the existence of thermite reactions between Al and NiO (that also result in alumina formation) [28,29], the fast growth of NiO most probably disturb the Al diffusion towards the substrate while preventing the formation of Ni_xAl_y intermetallic phases by reaction between the Ni substrate and the Al melt at 700°C. Therefore, most of the mass gain is related to the peripheral oxidation of Al microparticles and to the thickening of the oxide shells upon exposure to Ar-10%H_2O. Note that a fraction of the mass gain must also come from the growth of the TGO (i.e. α-Al_2O_3) in both synthetic air and Ar-10%H_2O. Simultaneously, more Al remained in the top coatings for the samples heat treated in Ar-10%H_2O (**Figure 6**) whereas fewer diffusion islands were observed (**Figures 5c** and **5f**). These phenomena probably arose because water vapour delays the opening of the microparticles like Pedraza and Podor demonstrated by in situ SEM in 120 Pa of H_2O and 120 Pa of synthetic air [8].

Nevertheless, the oxide shells observed after the complete heat treatment in water vapour appeared to be as thick as the ones obtained in synthetic air (**Figure 9**). When performing the heat treatment in Ar-10%H_2O, the diffusion islands were systematically surrounded by a thick α-Al_2O_3 TGO although the substrate remained unoxidized (**Figures 9c** and **9f**). The reasons why NiO grew under synthetic air and not in Ar-10%H_2O are still not fully understood since Rudolphi and Schütze have shown very minor differences between NiO grown at 800°C under dry and wet (10 and 30%H_2O) air [30]. Probably, the differences relate to the faster growth of the NiO scales in water vapour. This would induce further defects in the microstructure according to the SEM in situ observations at 700°C [31] through which Al can diffuse and react following thermite reactions [28,29].

4.2. Hybrid atmosphere: optimizing the formation of TBC systems in a single heat treatment

Using a single atmosphere for the heat treatment did not allow to obtain both a homogeneous aluminide coating and a thick and adherent top coating (see section 4.1.). The purpose of the hybrid atmosphere was therefore to procure enough diffusion of Al to form a homogeneous diffusion coating while promoting the peripheral oxidation of the Al microparticles in order to increase the strength of the top coatings. Thus, inert atmosphere was employed during the first part of the heat treatment to allow the initiation of the Al-Ni reaction [2,3,20]. Then, the introduction of an oxidizing atmosphere (i.e. synthetic

air or Ar-10%H_2O) was realized to oxidize the Al left in the microparticles hence, to thicken the alumina shells while simultaneously promoting the formation of α-Al_2O_3 TGO [1,4].

Regardless of the introduction temperature, both synthetic air and Ar-10%H_2O considerably increased the oxidation rate of the pure nickel/slurry system (**Figures 12** and **14**). As observed for the full heat treatment in synthetic air and in Ar-10%H_2O, a two-step oxidation curve was obtained for all conditions. These results are much in line with the works of Trunov et al., where the authors identified different stages of oxidation for Al microparticles heated in air by thermogravimetric analysis [15,19]. Up to 4 stages where thus identified upon heating [19]: i) ambient-400°C: desorption of water and dehydroxylation of the amorphous layer (slight decrease of mass) followed by the growth of the amorphous alumina layer (slight increase of mass), ii) 450-650°C: stepwise oxidation associated with the crystallization of the amorphous layer into γ-Al_2O_3 and its subsequent healing, iii) 650-950°C: second acceleration of the oxidation rate attributed to the growth of the γ-Al_2O_3 layer and by further crystallographic transformations (either γ-Al_2O_3 → δ-Al_2O_3 → θ-Al_2O_3 → α-Al_2O_3 [17,32,33] or γ-Al_2O_3 → α-Al_2O_3 [15,17,27] sequences) and iv) 950-1200°C: sharp decrease in the oxidation rate when the oxide shell is fully transformed into α-Al_2O_3 and progressive growth of α-Al_2O_3. Since no marked evolution is observed on the mass gain curve obtained in Ar (**Figure 12**), this indicates that the peripheral growth of the oxide shells was considerably limited in this atmosphere. Contrarily, the systematic stepwise oxidation observed right after introduction of synthetic air or Ar-10%H_2O (**Figures 12** and **14**, respectively) suggest that both oxidizing atmospheres fostered the crystallization and the growth of γ-Al_2O_3 [19]. It has to be noted that the particle size has a strong influence on the onset of the crystallization as observed by Kolarik et al. where the transformation of the amorphous alumina layer into γ-Al_2O_3 was detected by in-situ HT-XRD measurements from about 425°C for 0.3-0.7 µm particles to about 550°C for 2-5 µm particles [26]. This could explain why the larger Al microparticles tend to release more Al whereas the smaller ones are more oxidized and still filled with Al (**Figure 6**).

However, even though a systematic stepwise oxidation was observed after introduction of synthetic air, the earlier its introduction, the greater the mass gained after the diffusion step (**Figure 12**). This mass gain was far less marked with Ar-10%H_2O (**Figure 14**). The differences can be ascribed to two concurrent mechanisms: i) peripheral oxidation of the Al microspheres and thickening of the alumina shells as explained earlier and ii) oxidation of the nickel substrate. Since synthetic air fosters the oxidation of Ni with increasing temperature and NiO was barely detected in Ar-10%H_2O (**Figure 4**), it derives that the major contributor of the mass gain is the oxidation of Ni.

Upon heating between 700 and 1100°C, a second stepwise oxidation is systematically observed in all conditions (**Figures 12** and **14**). For the samples heat treated in Ar then in synthetic air (**Figure 12**), the introduction temperature strongly affected the mass gain values. When synthetic air is introduced at 550 or 600°C, the mass gain values are comparable to the ones obtained for the samples exposed to synthetic air only. This is consistent with the observations of the cross-sections (**Figs 11a** and **11d**) since the formation of NiO during the diffusion step blocks the inward diffusion of Al upon further annealing. Therefore, the Al that was left in the top coatings after the diffusion step (illustrated in **Figures 5b** and **5e**) oxidized and increased the level of sintering of the top coatings. When the temperature reaches 1100°C, the oxidation rate decreases, which probably indicates the predominant growth of α-Al_2O_3 [19]. The heterogenous diffusion layers obtained after introduction of synthetic air at 600°C and the presence of NiO at the intermetallic/top coating interface (**Figures 11a** and **11d**) resulted in a poor adherence of the top coatings for both types of microparticles, which was even shown to spall from the substrate for the Al_HS sample.

By further delaying the introduction of synthetic air at 650°C, the mass gain values are more than twice lower after the complete heat treatment (**Figure 12**). It therefore appeared that the Al left in the microparticles mostly reacted with pure nickel to form continuous nickel aluminide coatings since NiO did not form a barrier in this condition (**Figures 11b** and **11e**). However, the higher mass gain values than the ones obtained in Ar also suggest that the introduction of synthetic air before the complete emptying of the microparticles triggered the thickening of the alumina shells. The growth of a relatively thick α-Al_2O_3 TGO could also explain the second stepwise oxidation observed in such condition. Finally, when synthetic air is introduced at 700°C, a large fraction of the Al microparticles had already reacted with the pure nickel substrate to form nickel aluminides and less Al was left in the top coating for the thickening of the shells (**Figures 11c** and **11f**). This is emphasized in **Figure 12** with smaller stepwise oxidation. This resulted in the formation of top coatings with microstructures comparable to the ones obtained after the complete heat treatment in Ar (**Figures 9a** and **9d**).

The changes in the formation of the coatings with the introduction of Ar-10%H_2O at 650 and 700°C can be explained with the results of **Figure 14**. On the one hand, the late introduction of Ar-10%H_2O at 700°C allows Al to be supplied from the particles and react with the substrate. Therefore, there is little matter left to get oxidized compared to the introduction at 650°C. This would explain the thinner walls of the particles of the top coating and its subsequent shrinkage and the lesser oxidation of the diffusion layers (**Figures 13b** and **13d**) compared to the coatings obtained with the introduction of Ar-10%H_2O at 650°C (**Figures 13a** and **13c**). As such, the shell of the particles of the top coating appear thicker and the top coating itself is thicker (~30 and ~50 µm) than at 700°C (~20 µm). On the other hand, the higher

mass gain values recorded after introduction of Ar-10% H_2O at 650°C than the ones obtained after introduction at 700°C can only be attributed to the oxidation of Al since Ni cannot oxidize in this atmosphere (p_{O_2} ~ 0.05 atm). Therefore, no NiO could be detected in Ar-10%H_2O as opposed to the switch of the atmosphere with synthetic air (p_{O_2} ~ 0.2 atm). Note that the significant formation of α-Al_2O_3 within the diffusion layers (**Figures 13a**, **13b** and **12c**) had also an effect on the overall mass gain of the samples.

Finally, the comparison of **Figures 12** and **14** indicates that the mass gain values were more than two times higher after introduction of Ar-10%H_2O at both 650 and 700°C than after introduction of synthetic air. This highlights the beneficial influence of water vapour on the peripheral oxidation of the microspheres and on the thickening of the alumina shells as observed in **Figures 6** and **7** and reported in the work of Pedraza and Podor in Ref. [8].

5. Conclusions

This work presented the mechanisms of formation of full thermal barrier coating systems (aluminide coating, thermally grown oxide and thermal barrier top coating) from micro-sized Al particles on pure nickel. Depending on the atmosphere composition, different microstructures were obtained after a diffusion step (700°C-2 h) or a complete heat treatment (700°C-2 h + 1100°C-2 h). Whereas fast consumption of Al occurred in Ar to form the nickel aluminides, synthetic air and water vapour fostered the peripheral oxidation of Al micro-sized particles that impeded the release of Al and its diffusion towards the substrate. This resulted in heterogeneous diffusion layers but thicker top coatings with better sintering and thicker alumina shells. By using hybrid atmospheres, a good compromise for thickening the alumina shells and having a homogeneous aluminide coating was found when the oxidizing atmosphere was introduced at 650°C for synthetic air and at 700°C for Ar-10%H_2O atmosphere. Further work will be conducted in order to assess the mechanical resistance and the thermal insulation of the different top coatings achieved.

REFERENCES

1. X. Montero, M.C. Galetz, M. Schütze, Surf. Coat. Technol. 206 (2011) 1586-1594.

2. F. Pedraza, M. Mollard, B. Rannou, J. Balmain, B. Bouchaud, G. Bonnet, Mater. Chem. Phys. 134 (2012) 700-705.

3. B. Bouchaud, B. Rannou, F. Pedraza, Mater. Chem. Phys. 143 (2013) 416-424.

4. V. Kolarik, R. Roussel, M. Juez Lorenzo, H. Fietzek, Mater. High Temp. 29 (2012) 89-94.

5. F. Pedraza, M. Mollard, B. Rannou, B. Bouchaud, J. Balmain, G. Bonnet, Oxid. Met. 85 (2016) 231-244.

6. F. Pedraza, B. Rannou, G. Boissonnet, B. Bouchaud, Z. Maache-Rezzoug, J. Mat. Sci. Chem. Eng. 3 (2015) 17-22.

7. F. Pedraza, G. Boissonnet, B. Fernandez, B. Bouchaud, R. Podor, Int. Conference on Metallurgical Coatings and Thin Films, San Diego, USA, April 25-28, 2016.

8. F. Pedraza, R. Podor, Mater. Charact. 113 (2016) 198-206.

9. S. Hasani, M. Panjepour, M. Shamanian, Oxid. Met. 78 (2012) 179-195.

10. V.I. Levitas, B.W. Asay, S.F. Son, M. Pantoya, J. Appl. Phys. 101 (2007) 083524-1-20.

11. V.I. Levitas, M. Pantoya, K.W. Watson, Appl. Phys. Lett. 92 (2008) 201917-1-3.

12. V.I. Levitas, Phil. Trans. R. Soc. A 371 (2013) 1-14.

13. B. Rufino, F. Boulc'h, M.V. Coulet, G. Lacroix, R. Denoyel, Acta Mater. 55 (2007) 2815-2827.

14. L.P.H. Jeurgens, W.G. Sloof, F.D. Tichelaar, E.J. Mittemeijer, Thin Solid Films 418 (2002) 89-101.

15. M.A. Trunov, M. Schoenitz, X. Zun, E.L. Dreizin, Combust. Flame 140 (2005) 310-318.

16. B. Rufino, M.V. Coulet, R. Bouchet, O. Isnard, R. Denoyel, Acta Mater. 58 (2010) 4224-4232.

17. I. Levin, D. Brandon, J. Am. Ceram. Soc. 81 (1998) 1995-2012.

18. A. Rai, D. Lee, K. Park, M.R. Zachariah, J. Phys. Chem. B 108 (2004) 14793-14795.

19. M.A. Trunov, M. Schoenitz, E.L. Dreizin, Combust. Theory Model. 10 (2006) 603-623.

20. M.C. Galetz, X. Montero, M. Mollard, M. Gunthner, F. Pedraza, M. Schütze, Intermetallics 44 (2014) 8-17.

21. S. Hasani, A.P. Soleymani, M. Panjepour, A. Ghaei, Oxid. Met. 82 (2014) 209-224.

22. B. Rannou, F. Velasco, S. Guzmán, V. Kolarik, F. Pedraza, Mat. Chem. Phys. 134 (2012) 360-365.

23. G.W. Goward, D.H. Boone, Oxid. Met. 3 (1971) 475-495.

24. D.K. Das, V. Singh, S.V. Joshi, Metall. Mater. Trans. A 29 (1998) 2173-2188.

25. J. Angenete, K. Stiller, Surf. Coat. Technol. 150 (2002) 107-118.

26. V. Kolarik, M. Juez Lorenzo, H. Fietzek, Mater. Sci. Forum 696 (2011) 290-295.

27. F. Velasco, S. Guzman, C. Moral, A. Bautista, Oxid. Met. 80 (2013) 403-422.

28. D. Vrel, P. Langlois, E.M. Heian, N. Karnatak, S. Dubois, M.F. Beaufort, Intnal. J. Self-Propag. High-Temp. Synth. 12 (2003) 261-270.

29. D. Vrel, A. Hendaoui, P. Langlois, S. Dubois, V. Gauthier, B. Cochepin, Intnal. J. Self-Propag. High-Temp. Synth. 16 (2007) 62-69.

30. M. Rudolphi, M. Schütze, *Moisture Induced Damage in Oxide Scales*, https://gfkorr.de/kwi_media/Downloads/hochtemperaturwerkstoffe/Projekte/high_temperature_materi als_poster_moisture_damage.pdf, accessed to 31/01/2019

31. B. Schmid, N. Aas, Ø. Grong, R. Ødegaard, Scanning 23 (2001) 255-266.

32. C.S. Nordahl, G.L. Messing, J. Eur. Ceram. Soc. 22 (2002) 415-422.

33. M. Bodaghi, A.R. Mirhabibi, H. Zolfonum, M. Tahriri, M. Karimi, Phase Transit. 81 (2008) 571-580.